Supplementary Information

Intrinsic structure perspective for MIPS interfaces in systems of ABP
Enrique Chacón[a], Francisco Alarcón[b,e] , Jorge Ramirez[c], Pedro Tarazona[d] and Chantal Valeriani[e]

a) *Instituto de Ciencia de Materiales de Madrid, CSIC, 28049 Madrid, Spain*
b) *Departamento de Ingeniería Física, División de Ciencias e Ingenierías, Universidad de Guanajuato, Loma del Bosque 103, 37150 León, Mexico.*
c) *Departamento de Ingenieria Quimica, ETSI Industriales, Universidad Politecnica de Madrid, 28006 Madrid*
d) *Departamento de Física Teórica de la Materia Condensada, Condensed Matter Physics Center (IFIMAC), Universidad Autonoma de Madrid, 28049 Madrid, Spain*
e) *Departamento de Estructura de la Materia, Física Térmica y Electrónica, Facultad de Ciencias Físicas, Universidad Complutense de Madrid, 28040, Madrid, Spain.*

1.- Numerical Simulations

1.1 Construction of a liquid-vapor phase coexistence at equilibrium for the passive LJ fluid.

Starting from previous work [1], where the vapour-liquid equilibria of a 2D passive LJ fluid is studied by means of Monte Carlo simulations in the Gibbs ensemble, we have used the proposed phase diagram as a starting point to get a liquid-gas phase coexistence in equilibrium easily. The problem is to generate a liquid-vapor slab that remains stable when the activity is introduced. With that goal in mind, we have carried out a couple of molecular dynamics simulations in two different ensembles at equilibrium for a passive LJ fluid (cut & shifted) with a cut-off range of 2.5σ:

$$V(r) = 4\varepsilon \left(\left(\frac{\sigma}{r}\right)^{12} - \left(\frac{\sigma}{r}\right)^{6} \right) \qquad\qquad r \leq 2.5\sigma$$

1. We have run classical molecular dynamics in the NPT ensemble [2] at different values of T and P where phase coexistence has been seen previously [1]. In all the tests, we start the simulations from the initial configuration shown on the left side of Fig. 1, using a square box of $L = 212\sigma$. After all the simulations were analysed, we kept with the case (P,T) where the liquid band was more stable. The most stable band is found at $P = 0.015$ and $T = 0.42\varepsilon$, and the simulation box is modified from the initial square geometry to a rectangular box of size $L_x = 677.39\sigma$ and $L_y = 152.83\sigma$,

2. Starting from the output configuration of the previous step (centre snapshot of Fig. 1), we have run an MD simulation in the NVT ensemble in order to test the stability of the liquid band. In the snapshot at the right of Fig. 1, the final configuration of such simulation can be observed. The mean number density in the inner part of the liquid slab is $\rho\sigma^2 = 0.386$.
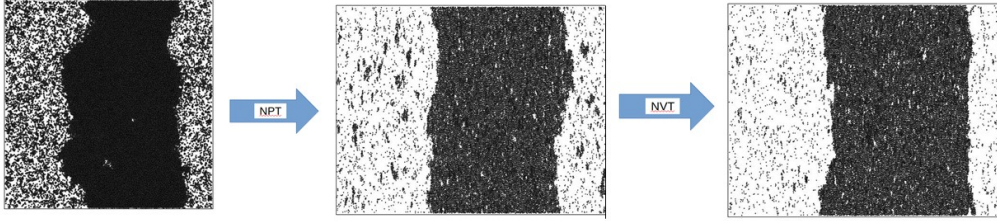
Fig1.- Graphical scheme of the protocol to get liquid-vapour phase coexistence at equilibrium. Left: initial configuration used in the MD simulations in NPT ensemble. Center: final configuration after an NPT simulation, at P=0.015 and T=0.42 , and initial configurations for the NVT simulations. Right: final configuration after an NVT simulation. In all the simulations N=40000.

1.2 Construction of a high-low density phase coexistence with attractive ABPs

Once we have tested the stability of the band of a passive LJ-liquid at equilibrium, we introduce the activity to the LJ-liquid systematically. In addition to the LJ interaction, all particles have a self-propulsion velocity and follow equations 1 and 2 of the main text.

For the different F_a values, the temperature $k_B T = 0.42$ was kept constant and the same initial configuration, which corresponds to the last configuration of the equilibrium passive LJ (right snapshot of Fig. 1), was used.

Similarly to previous studies [3], we have also observed that for the attractive ABP (ABP-LJ) system a reentrant phase behavior appears with respect to the band stability. For small values of activity we see that the band is stable, as long as $F_a < 3$ (see Fig. 2).
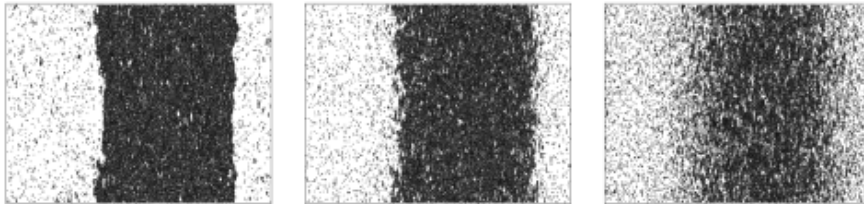

Fig 2. Snapshots of the last frame of simulations, using attractive ABPs with F_a = {0.1, 1, 3} respectively.

However, if the particles self-propel at medium speed i.e. $3 < F_a < 50$, the band melts and a homogeneous gas phase is observed. Strikingly, when the self-propulsion velocity is increased even further ($F_a > 40$), phase coexistence emerges again, and a more compact band is formed (see Fig. 3).
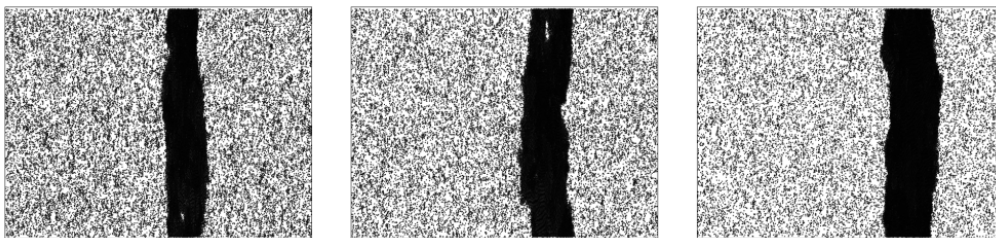

Fig 3. Snapshots of the last frame of simulations, using attractive ABPs with F_a = {50, 60, 80} respectively.

The evolution of the internal energy per particle for the attractive ABP to high F_a is:
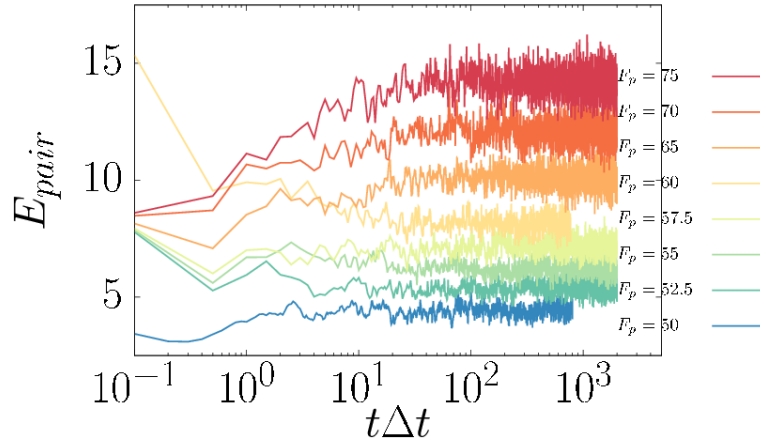

Fig 4. Left panel: Evolution of the internal energy per particle for the attractive ABP (ABP-LJ) system.

In summary, we have obtained the phase coexistence for three different systems. In the one hand, a system in thermal equilibrium of a passive LJ-particles by using MD simulations with help of two different ensembles (Fig. 1). In the other hand, a system of attractive ABPs out of equilibrium where the phase coexistence is obtained at low (Fig. 2) and at high self-propulsion speeds (Fig. 3) of the particles.

1.3 Construction of a high-low density phase coexistence with repulsive ABPs

Additionally, we have run NVT simulations of repulsive ABPs (ABP-WCA) using the same simulation box and density, and starting from the last configuration of the NPT simulation at equilibrium, resulting in the formation of a condensed band, as observed in Fig. 5. Note that the bands formed at high speeds are quite similar to those formed by MIPS of repulsive ABPs. In this case, particles are purely repulsive with a WCA potential:

$$V(r) = 4\varepsilon \left(\left(\frac{\sigma}{r} \right)^{12} - \left(\frac{\sigma}{r} \right)^6 \right) + \epsilon \qquad\qquad r \leq 2^{\frac{1}{6}}\sigma$$
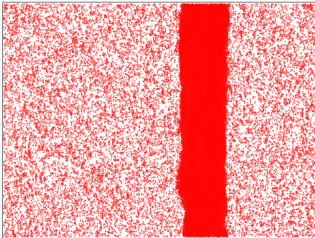

Fig 5. Snapshot of the last frame of a simulation, of repulsive ABPs with a WCA potential, with $F_a = 60$, T= 0.42 and ρ = 0.38..

Mean results

In the following graph, we show the mean density profiles at high Péclet number ($F_a > 50$)

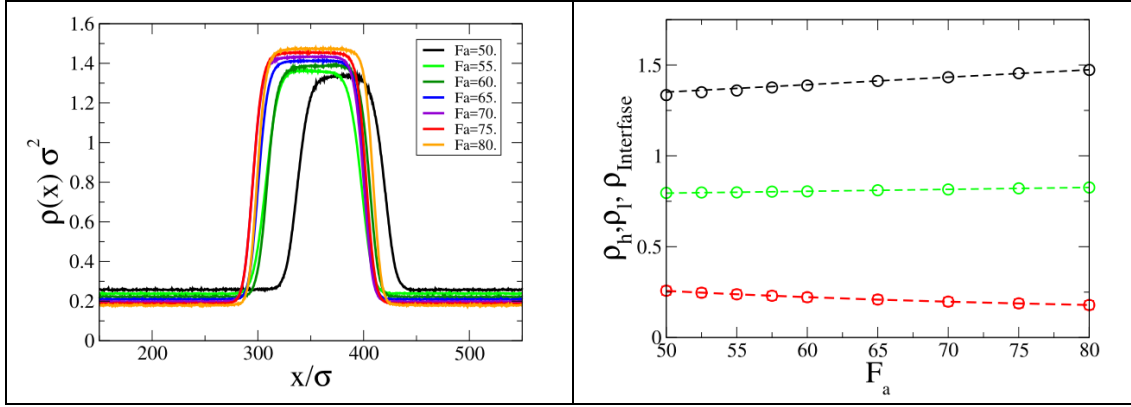$$\rho(x) = \left\langle \sum_i \delta(x - x_i) \right\rangle \Big/ L_y$$

Fig 6. Left panel: The mean density profiles for the ABP-LJ systems. Right panel: The equilibrium coexistent bulk densities, black:ρ_h dense phase, red: ρ_l diluite phase and rreen: $\rho_{Interphase} = \frac{\rho_h + \rho_l}{2}$

As we can see at these high activities, the densities of coexistence change with the activity. With respect to the densities of the coexisting phases, the effect of increasing the activity is equivalent to that of lowering the temperature in an LJ fluid, increasing the density of the dense (condensed) phase and decreasing the density of the dilute (non-condensed) phase.
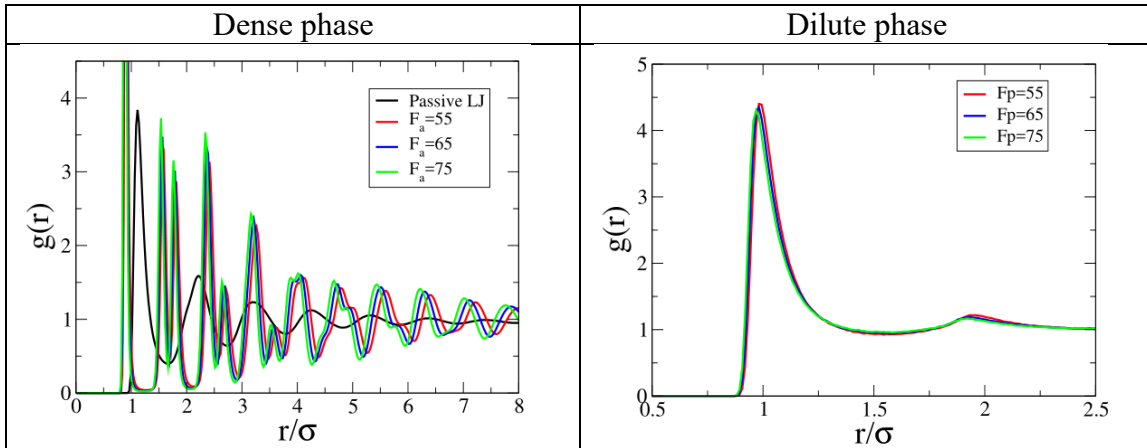

Fig.7.- Left panel: The radial distribution function of the bulk dense phase of the ABP-LJ, measured in the central part of the dense slab. Right panel: the structure factor of the bulk dilute phase.

The radial distribution function $g(r)$ of the dense coexisting phase at high F_a shows a solid-like structure for the first shell, with strong 6-fold correlation of the nearest neighbour particles, and a liquid structure at large range. The oscillations of $g(r)$ shift very slightly towards smaller r's when we increase F_a while also slightly increasing its structuring. If we compare with the $g(r)$ of the liquid phase of the non-active LJ we see that the high activity significantly pushes the particles towards the repulsive part of their interaction potentials. The position of these peaks (and the high average density) makes it clear that for these high values of F_a the attractive part of the LJ potential is irrelevant, because the neighbors are at distances with very strong repulsion. So the mean nearest neighbor (nn) distance $\langle d_{nn} \rangle$ decreases slightly when we increase F_a. In the right panel of Fig. 6 we can see that the dense slab has nearly constant density,

very close to the perfect triangular lattice $\rho = 2/(\sqrt{3}\langle d_{nn}\rangle^2)$, so that the crystal defects give only a very small correction.

The density (or mean nn distance) over the crystalline regions of the dense slab provides a natural scale (at each F_a) that gives an interesting view to the MIPS coexisting densities . Fig. 8 presents the densities in LJ units (left), together with the usual analysis (as it were a 2D liquid-vapor coexistence with $\beta = 1/8$ critical exponent) which may be misleading, since the coexisting densities are too different. On the right panel of the figure, a rather different view appears when we scale the densities with $\langle d_{nn}\rangle$. The gas density follows very well a simple law $\rho_l = 11.1/(\langle d_{nn}\rangle^2 F_a)$, with 11.1 as the only fitting parameter. Apparently, most of the explored F_a range is more simply described by a 'high activity' approximation, while the 'critical region' description is much more forced (it requires more free parameters, and fits the results too much away from the apparent critical value of F_a).
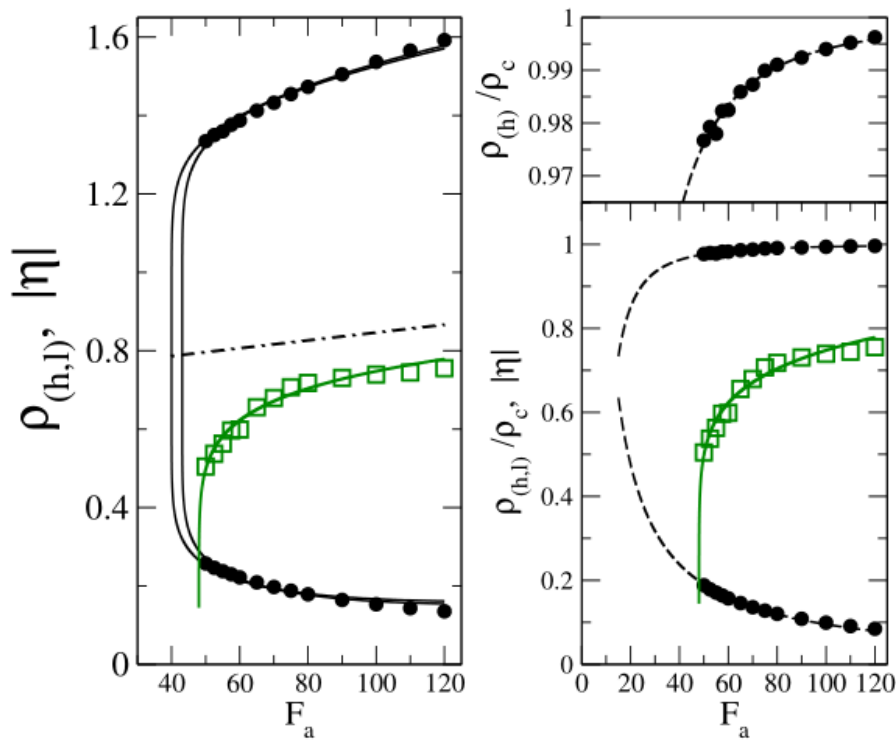

Fig 8. Full black circles: coexisting MIPS densities, ABP-LJ results for $50 \leq F_a \leq 80$ and ABP-WCA results for $F_a > 80$. Left: in LJ units, and fitted as a 2D critical region, with Ising critical exponent $\beta = 1/8$ and two critical values $F_a^c = 40$ and 43. Right: density scaled in the crystalline density $\rho_c = 2/(\sqrt{3}\langle d_{nn}(F_a)\rangle^2)$ and (dashed lines) their fits to $\frac{\rho_h}{\rho_c} = 1 - 60/F_a^2$ and $\frac{\rho_h}{\rho_c} = 9.52/F_a$. Open green squares: the hexatic order parameter calculated over the crystalline sites in the dense slab, and (full green line) its fit to a critical behaviour with $\beta = 1/8$ and $F_a^c = 48$.

Intrinsic line

Actually, with the level of fluctuation in these 2D "active" simulations and in 2D, the most fine-grained methods designed for 3D interfaces are not very practical [4,5,6]. What we are using is a "less refined" but more robust version, which has also been used on normal liquid surfaces [7,8]. For each analysed configuration, we create a continuous "coarse-grained " density function $\rho(x, y)$ from the convolution of the particle positions with a Gaussian:

$$\rho(x,y) = \sum_{i=1}^{N_{particles}} \frac{1}{2\pi\alpha} e^{\frac{(x-x_i)^2+(y-y_i)^2}{2\alpha^2}}$$

Then we define the interfacial line $x = \xi(y)$ as that over which $\rho(x = \xi(y), y)$ is at the mean value of the two coexisting densities.

$$\rho(x = \xi(y), y) = \rho_{interface}$$

That line is made univaluated (at each side of the slab) by eliminating the small dense droplets and gas bubbles (i.e. closed contours of $x = \xi(y)$, as well as some -- very few -- overhangs).

Then, the Fourier components ξ_{n_y} can be obtained directly, using the periodic boundary conditions along the Y direction.

$$\xi(y) = \xi_0 + \sum_{n_y>0}^{n_y=n_u} \left(\xi_{n_y} cos(q_y y) + \xi_{-n_y} sin(q_y y) \right) \quad where \quad q_y = \frac{2\pi}{L_y} n_y$$

We have checked that the distribution of each ξ_{n_y} is very accurately Gaussian, with null mean value $\left\langle \xi_{n_y} \right\rangle = 0$ (very long simulation runs are required to good statistical sampling for the lowest q modes), and therefore the interfacial fluctuations are fully described by their mean square value $\left\langle \left| \xi_{n_y} \right|^2 \right\rangle$, that we obtained from 2000 configurations separated by 100000 time steps. We get separate statistics for the two sides of the slab ('left' and 'right' interfaces), to guarantee a good convergence, and both values may be employed to improve the statistics of the final results.

The upper limit $q_u = \frac{2\pi}{L_y} n_u \geq |q_y|$ used in the Fourier series controls how closely the nominal interfacial line $x = \xi(y)$ follows the position of the particles. To study how the intrinsic line depends on the value of q_u, we show in Fig. 9 an enlarged view of the surface on the right side of Figure 1 in the main article. As our intrinsic line is a continous function, our choice of q_u is very simple; it is the smallest value of q_u above which the setting ceases to depend appreciably on q_u, $n_u = 12$ in our case.
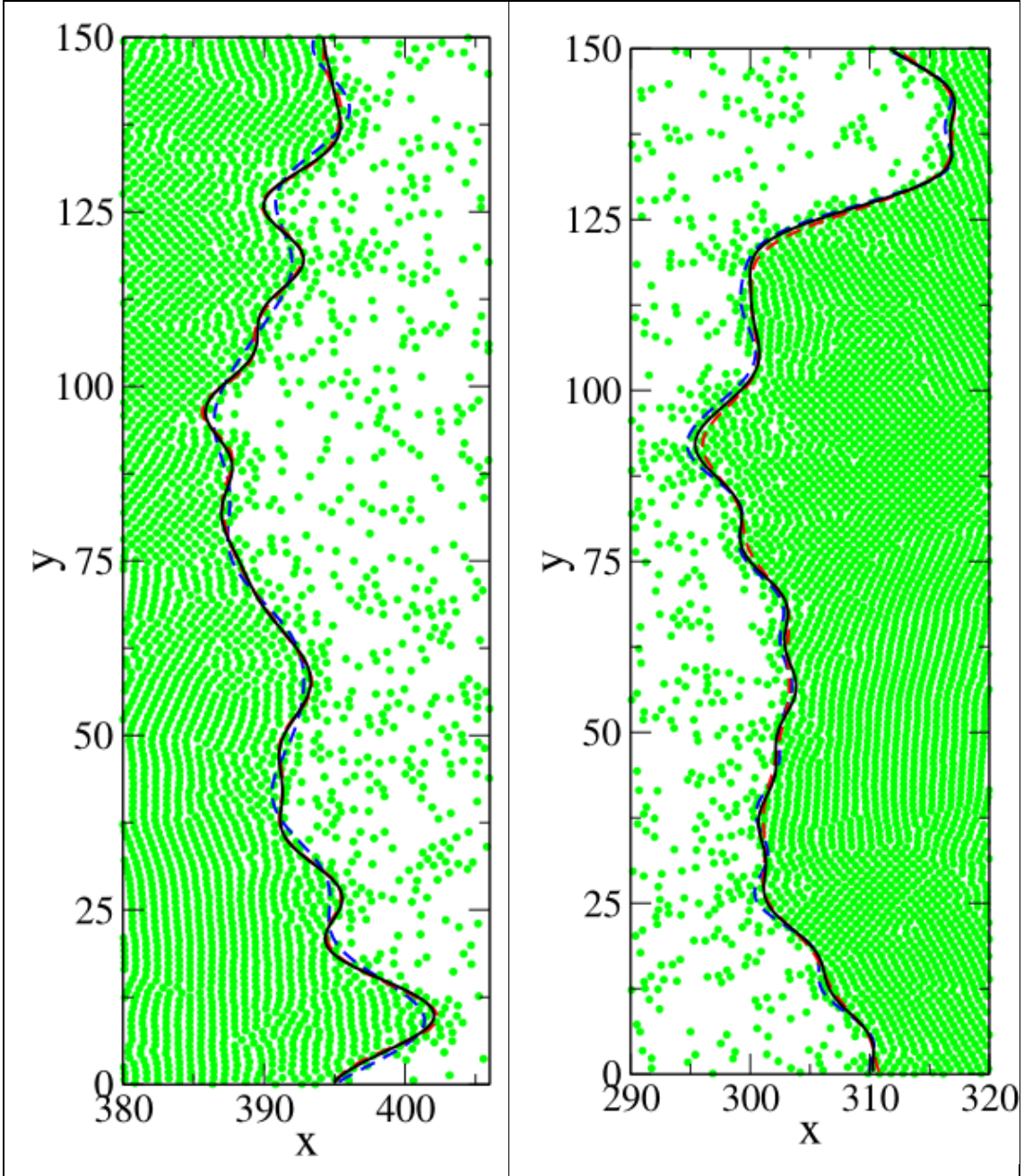
Fig 9. The intrinsic Surface of the ABP-LJ with $F_a = 55$ and $\alpha = 2$ for the Gaussian coarse-grained density. The black full-line corresponds to our preferred choice $q_u\sigma = 0.5$ of the upper cutoff in the Fourier series. The dashed lines shows the effects of changing q_u; $q_u\sigma = 0.25$ (blue) and $q_u\sigma = 1.75$ (red).

Fig. 10. The intrinsic Surface of the ABP-LJ with $F_a = 55$ and $q_u\sigma = 0.5$ as the upper cutoff in the Fourier series. The black full line correspond to our preferred choice $\alpha = 2$ for the Gaussian coarse-grained density. The dashed lines show $\alpha = 1$ (blue) and $\alpha = 3$ (red)

To study the dependence of the intrinsic line with the value of α we show in Fig.10 an enlarged view of the liquid-vapor interface on the right of Figure 1 in the main article. The choice of the optimal value of α is more delicate than the choice of the optimal value of q_u, so in the following sections we will analyze the dependence of the intrinsic profile and the spectrum of fluctuations with the choice of α.

Intrinsic density profile

As in the thermal equilibrium of fluid interfaces, the mean density profiles shown previously should depend on the transverse size of the system L_y, due to the blurring from local displacements of the interface ("capillary waves" CW). In 2D the interfacial width grows as L_y (in contrast with the much weaker effect $log(L_y)$ in 3D), so that there is not a thermodynamic limit ($L_y \to \infty$) for these mean density profiles. Borrowing the concepts of the Capillary Wave Theory (CWT) for equilibrium, a true thermodynamic limit may be obtained only for the intrinsic density profiles, defined as:

$$\rho_I(y) = \left\langle \left| \sum_i \delta(x - x_i + \xi(y_i)) \right| \right\rangle \Big/ L_y$$

In the next figure, we can see that the intrinsic profile depends only weakly on the value of α used. We have selected a value of $\alpha = 2$.
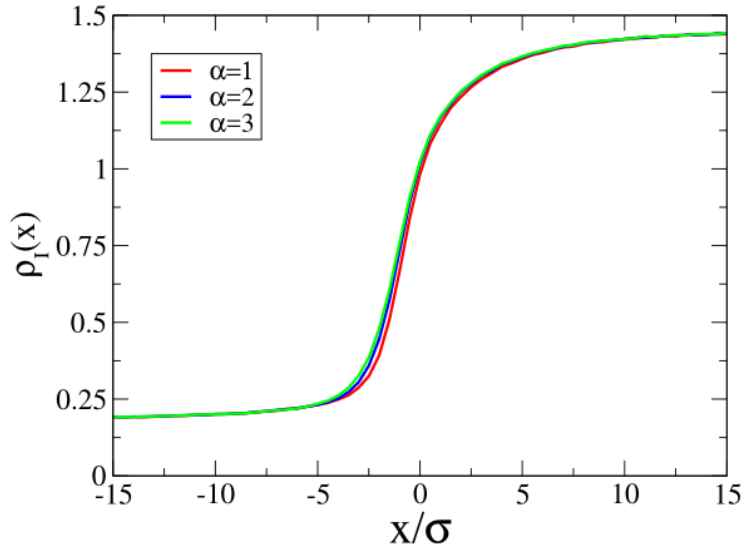

Fig. 11 Intrinsic profiles for Fa=75 with $q_u\sigma = 0.5$ as the upper cutoff in the Fourier series for the system ABP-LJ, using values of $\alpha = 1$ (red), $\alpha = 2$ (blue) and $\alpha = 3$ (green). Units of the LJ diameter are used.

If we compare the intrinsic profiles with the mean, the $\rho_I(x)$ (see Fig. 12) give a sharper (and size independent) view of the interfacial region, with a more rapid decay on the 'gas' side than on the dense side of the interface. The variation of $\rho_I(x)$ towards the bulk values is clearly slower at the dense side of the interface, with a rather thick interfacial region, x ≈ 15 − 20 particle diameters, over which the density is already high but still gradually increasing. On the 'gas' side the decay is also slow for the mean density for all values of F_a, but $\rho_I(x)$ decays faster, over two or three particle diameters. The fact that the intrinsic profiles are so clearly asymmetric suggests that the loss of phase separation is not due to the normal mechanism ("vapor bubbles" in the liquid and "liquid drops" in the vapor) but rather due to the loss of hexatic order, because the most relevant order parameter is the one that is only in one side. It is striking that, in the length units of the nearest neighbour distance $\langle d_{nm} \rangle (F_a)$ and over the entire range of explored F_a values , we get very similar density profiles, which collapse in a

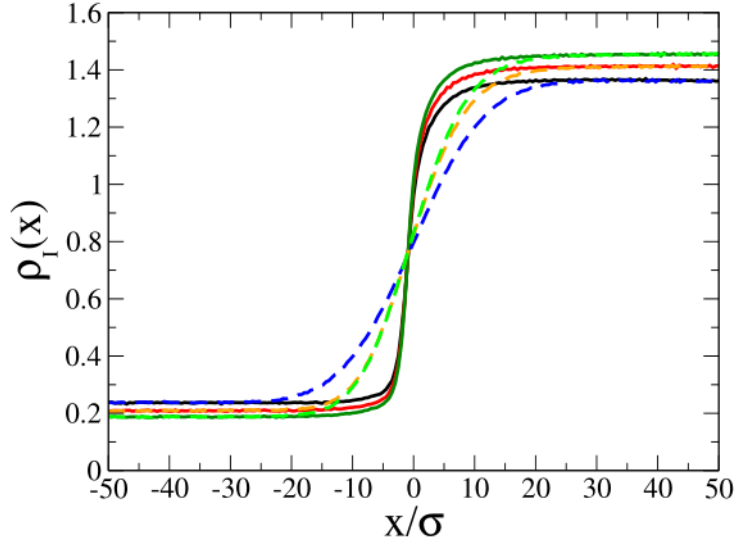single curve in terms of $(\rho_I(x) - \rho_h - \rho_l)/(\rho_h - \rho_l)$, as we can see in Fig.3 of the main text.

Fig. 12. Mean (dashed line) and intrinsic profiles (full lines) for Fa=55 (blue), 65 (red) and 75 (green) for the system ABP-LJ. Units of the LJ diameter are used.

Line tension from the fluctuations of the interfacial line

We shift now to the second part of the evidence extracted by the intrinsic analysis of the interface. The observed Gaussian distribution for the Fourier amplitudes ξ_{q_y} of the interfacial line $x = \xi(y)$ may be interpreted as that in an effective thermal equilibrium ensemble, with a line Hamiltonian $H[\xi_{q_x}]$ that may be represented in terms of a line tension γ_0 times the line length L[ξ], as a functional of the line shape, and expanded up to quadratic order in the Fourier amplitudes ξ_{q_y}, i.e.

$$L\left[\xi_{q_y}\right] \approx L_y\left(1 + \frac{1}{2}\sum_{q \neq 0} q_y^2 \left|\xi_{q_y}\right|^2\right)$$

The generalization to include curvature contributions, with bending modulus κ, in terms of a wavevector dependent line (surface) tension $\gamma(q_y) = \gamma_0 + \kappa q_y^2 + \cdots$ leads to an effective interfacial Hamiltonian, weighted with an effective temperature:

$$\beta H[q_y] = L_y\left(\beta\gamma_0 + \frac{1}{2}\sum_{q_y \neq 0} \beta\gamma(q_y)q_y^2 \left|\xi_{q_y}\right|^2\right)$$

that should give the independent Gaussian probability distributions for each Fourier amplitude an (effective) Boltzmann probability distribution, that for long wavelengths give a probability $\exp(\beta H[\xi])$ for any shape of the interfacial line, just in terms of the line length and the single parameter $\beta\gamma_0$, see panel (b) in Fig. 7.

Therefore, the mean square values$\left\langle \left| \xi_{q_y} \right|^2 \right\rangle$ obtained from the simulations (for any $q_y \neq$ 0) give directly:$\beta\gamma(q_y) = \dfrac{1}{L_y \left\langle \left| \xi_{q_y} \right|^2 \right\rangle q_y^2}$ to get $\beta\gamma_0$ as the $q = 0$ extrapolation, and $\beta\kappa$ from a quadratic fit at low q. For systems in true thermal equilibrium, this method to get $\beta\gamma_0$ is well tested and quite robust, while the estimation of the bending modulus is more subtle and depends on a (good) definition for the interfacial shape, from the positions of the particles. The results obtained for the MIPS interface are presented in the next figure:
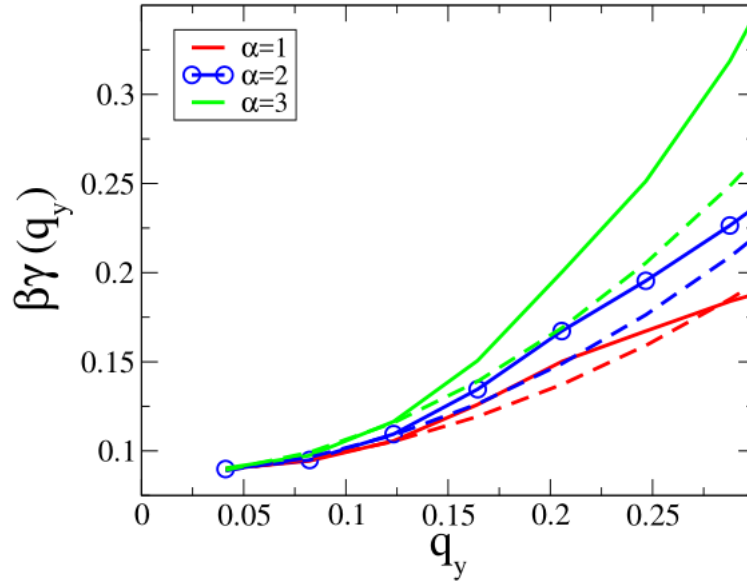

Fig.13. The function $\dfrac{1}{L_y \left\langle \left| \xi_{q_y} \right|^2 \right\rangle q_y^2}$ s with $q_u\sigma = 0.5$ as the upper cutoff in the Fourier serie for the system APB-LJ with $F_a = 75$. Units of the LJ diameter are used. Red line: $\alpha = 1$, blue line: $\alpha = 2$ and green line: $\alpha = 3$. The dashed lines are the fit to $\gamma(q_y) = \gamma_0 + \kappa q_y^2$ in the range $0 < q_y < 0.15$

As we can see, as in thermal systems, for the ABP the γ_0 is very well determined by the method, but the bending depends drastically on the details of the procedure; in particular, it varies a lot with the choice of the value of α. That is why in this work we have only focused on the discussion about $\beta\gamma_0$ and have avoided any discussion with respect to κ, given its dependence on the choice of α. However, a rough estimate of the ratio $\kappa/\gamma_0 \sim 18 \pm 5$ allows us to state that corrugations of interfacial line with wavelengths longer than ~ 100 particles diameters are quantitatively well described (with accuracy better than 90%) by the 'macroscopic equilibrium' prediction based only on the value of $\beta\gamma_0$ multiplied by the line length; i.e. the observed fluctuations in the shape of the MIPS interface have a probability distribution $P[\xi] \propto exp(-\beta\gamma_0 L[\xi])$, with an exponential decay in terms of the increase in the length of the line.

Note that the analysis of the fluctuations of the MIPS interfacial line does not give γ_0 but $\beta\gamma_0 = \gamma_0/kT_{eff}$, in terms of an effective temperature, which does not represent the 'normal' (and nearly irrelevant temperatures) set in the Brownian dynamics. But even without assuming an effective temperature, some interesting results appear from the analysis of $\beta\gamma_0$. Our results should be regarded more as an "effective thermodynamic"

than a "mechanical" calculation of the line tension. Nevertheless, at least in respect to its sign, we are sure to get $\gamma_0 > 0$, otherwise the interface would be unstable, and the method measures precisely its stability with respect to the fluctuations under stationary MIPS. Moreover, our approach has the advantage to get $\beta\gamma_0$ through a direct observation, within a well-tested method for thermal equilibrium interfaces, and had been used previously by Patch et al ref. [9].

F_a	$\beta\gamma_0^{Inf}$	$\beta\gamma_0^{Sup}$
50 (LJ)	0.0437	0.0490
52.5 (LJ)	0.0534	0.0542
55 (LJ)	0.0586	0.0541
57.5 (LJ)	0.0618	0.0661
60 (LJ)	0.0584	0.0712
60 (WCA)	0.0681	0.0646
65 (LJ)	0.0664	0.0748
70 (LJ)	0.0707	0.0769
70 (WCA)	0.0842	0.0790
75 (LJ)	0.0798	0.0883
80 (LJ)	0.0846	0.0879
80 (WCA)	0.0868	0.0876
90 (WCA)	0.0961	0.0844
100 (WCA)	0.0915	0.0941
110 (WCA)	0.0858	0.0881
120 (WCA)	0.0836	0.0732

A summary of our results is given in the table, where the first column represent the value of Fa for either LJ or WCA, the second column $\beta\gamma_0^{Inf}$ and the third column $\beta\gamma_0^{Sup}$

Hexatic order parameter

The triangular lattice coordination in the dense slab is measured by the local hexatic order parameter:

$$\eta_j = \sum_{k=nn} \frac{exp(6i\theta_k)}{6}$$

Where θ_k is the orientation of vector $\vec{r}_{jk} = \vec{r}_k - \vec{r}_j$ for the neighbors of particle j.

In the next two figures we can see the hexatic order parameter $\eta = \sum_j \eta_j / N = \eta_x + i\eta_y$ (one point for each configuration) represented as a vector (and the histogram of its square module that gives the mean value used in Fig. 5 of the main paper). ABP-LJ simulations at $50 < F_a < 80$ and ABP-WCA systems at $F_a \geq 80$ are shown in Fig. 14 and 15, respectively. As you can see at high F_a, a large and empty "doughnut shape" is formed, with a strong hexatic order whose direction (with respect to the slab axes) changes throughout the simulation. For lower F_a the "doughnut shape " becomes smaller and "filled", because the global hexatic order of each configuration is reduced: grains appear with different orientations, separated by disclinations.
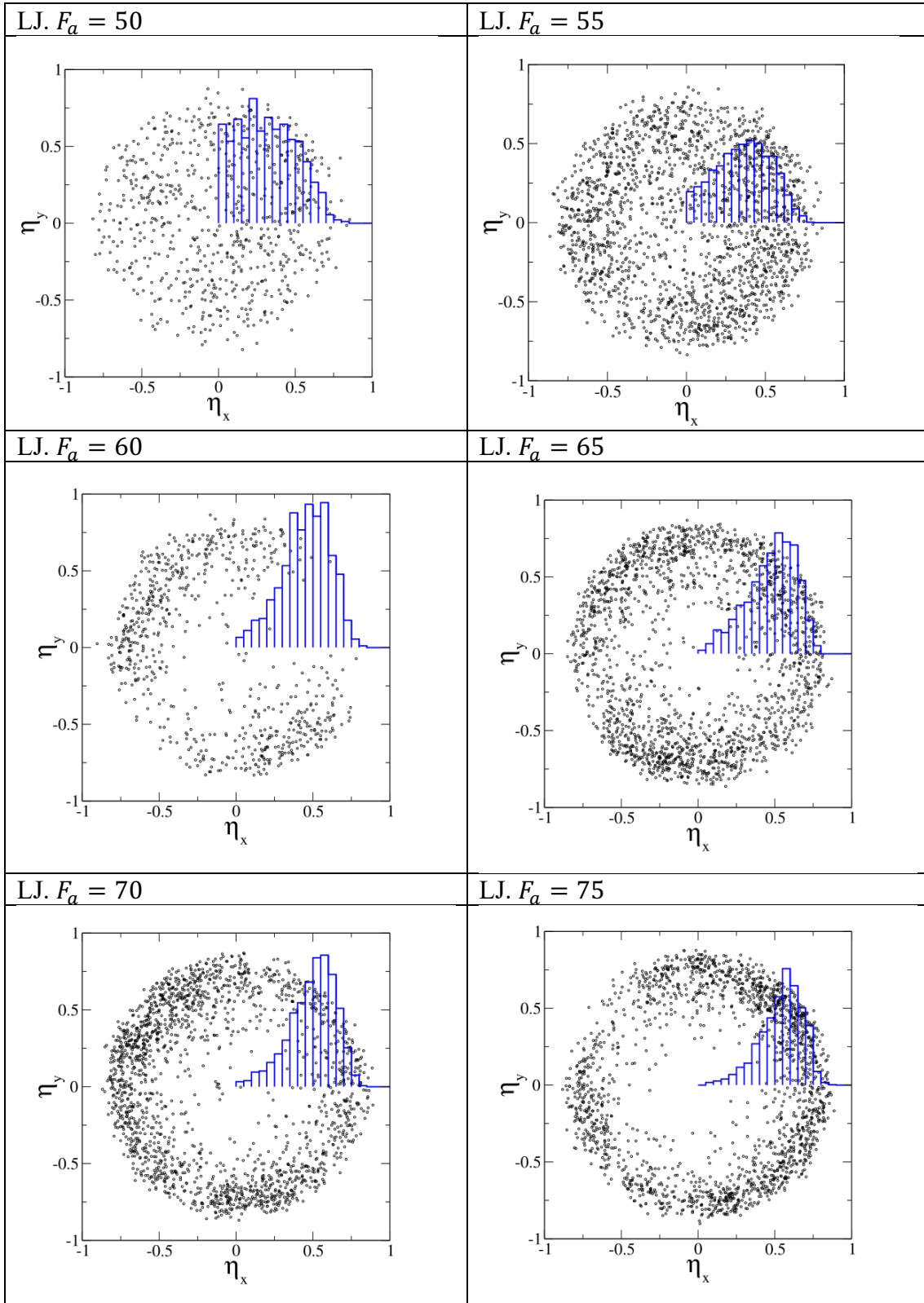
Fig.14.- The real part (η_x) versus the imaginary part (η_y) of the complex local hexatic order parameter of the ABP-LJ with $50 < F_a < 80$ at the inner part of the dense slab (one dot for each configuration). The blue lines are the histograms of the module $|\eta|$ whose integral gives the mean value of $\langle |\eta| \rangle$ represented in figure 5 of the main article.
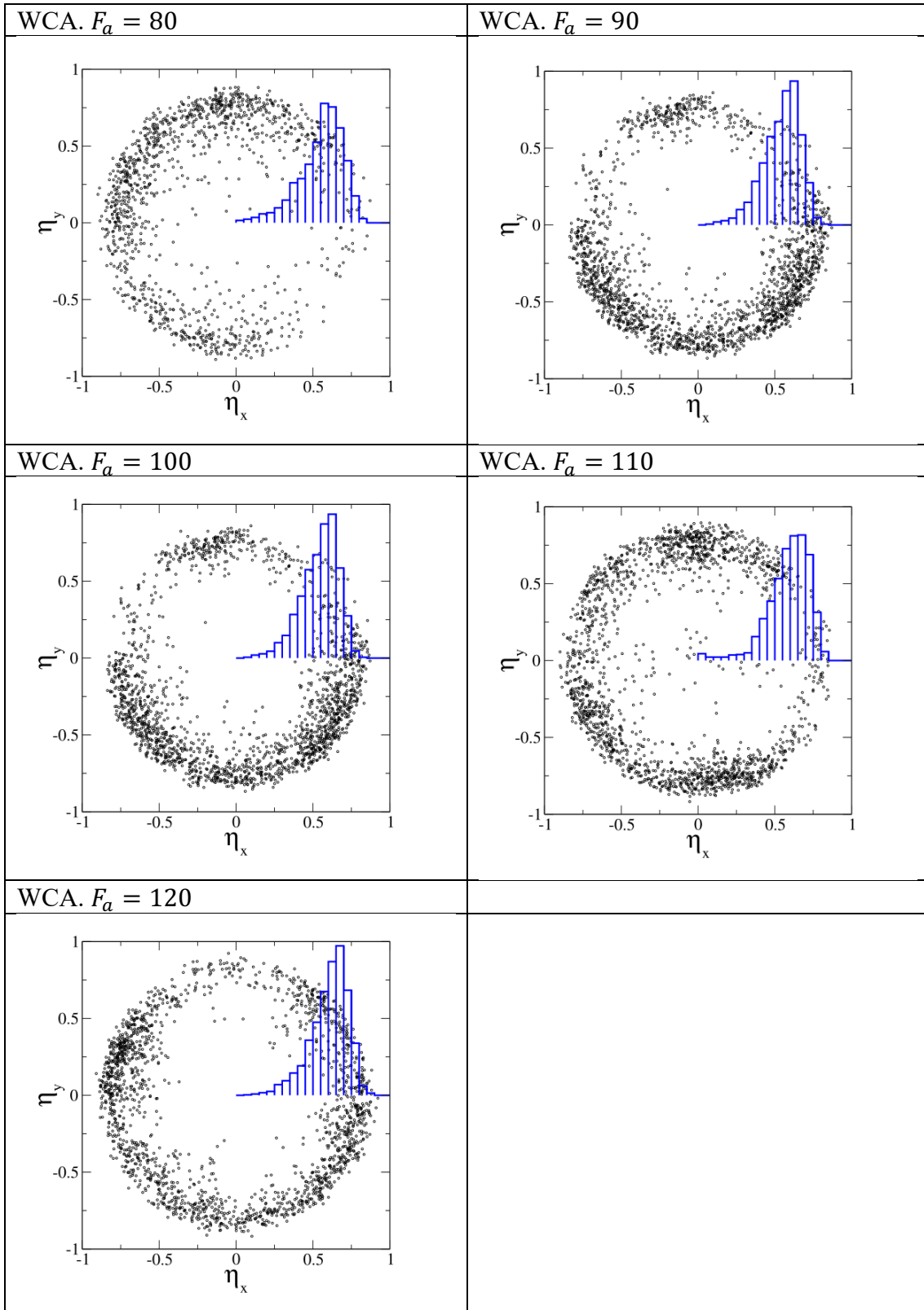
WCA. $F_a = 80$	WCA. $F_a = 90$
WCA. $F_a = 100$	WCA. $F_a = 110$
WCA. $F_a = 120$	

Fig.15.- The real part versus the imaginary part of the complex local hexatic order parameter for the ABP-WCA with $80 < F_a < 120$., at the inner part of the dense slab. The blue lines are the histograms of the module $|\eta|$ whose integral gives the mean value of $\langle|\eta|\rangle$ represented in figure 5 of the main article

Time correlations of the Fourier amplitudes of the intrinsic line.

Finally, we have studied the exponential decay time of the auto-correlation of the Fourier amplitudes of the intrinsic line:

$$c(t) = \langle \xi_q(t_0)\xi_{-q}(t - t_0) \rangle = \left\langle \left| \xi_q \right|^2 \right\rangle e^{-t/\tau_q}$$

The typical time scale for interfacial fluctuations is set by the active force F_a (as it would be set by $k_B T$ in a thermal equilibrium system) and the linear dependence with q_y is compatible with the limit of overdamped dynamics. The required simulation times to explore the steady state of a MIPS slab would be proportional to L_y/F_a, to allow for good statistical sampling of the slowest ($q_y = 2\pi n_y/L_y$) interfacial fluctuations.

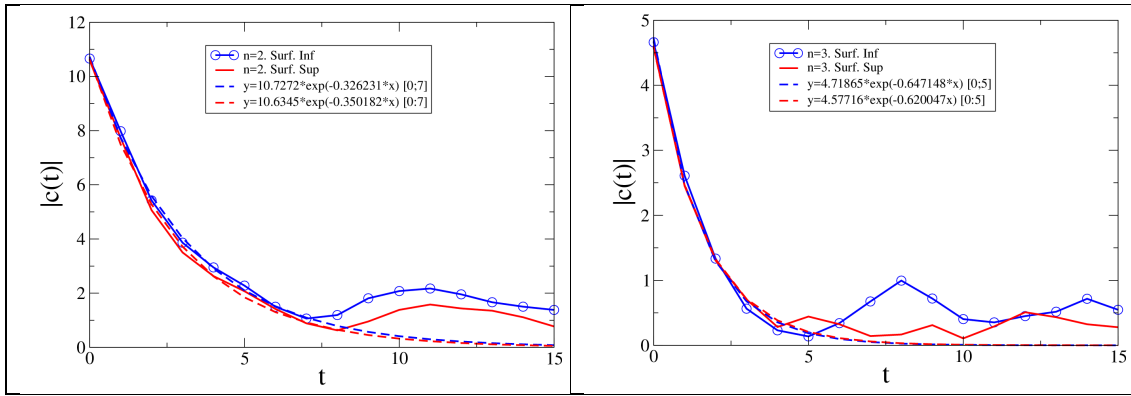As we can see in the next figures the numerical results can be well fitted by an exponential decay.

Fig.16.- Auto-correlation of the amplitudes of the intrinsic lines for the ABP-LJ system with $F_a = 60$ and $\alpha = 2$. Left panel: $n_y = 2$, right panel: $n_y = 3$. The time unit is 2000 times the time step. Inf surface(blue), Sup (red).

In the next figure we show the exponential decay time of the auto-correlation of the Fourier amplitudes of the intrinsic line $\tau(q_y)$ for several values of F_a:
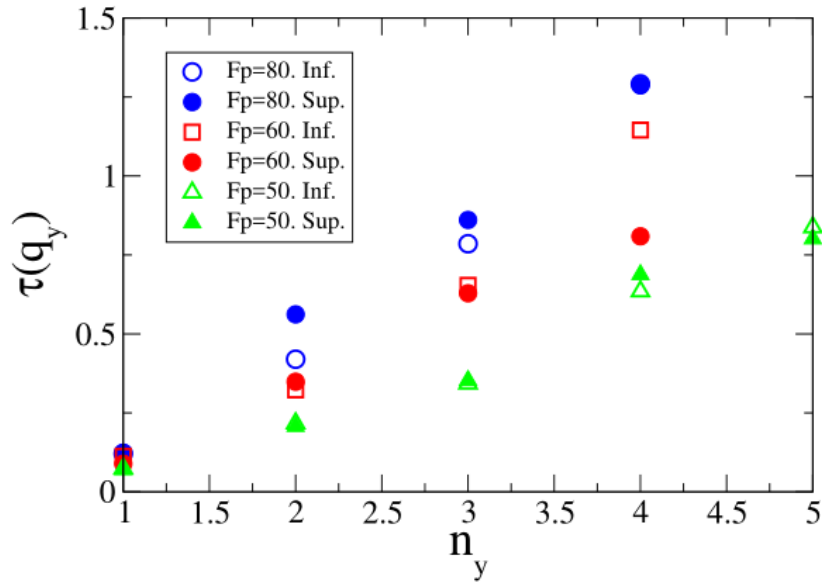
Fig.17.- The decay time of the auto-correlation of the amplitudes of the intrinsic lines for the ABP-LJ system for several values of F_a=80 (blue), $F_a = 60$ (red) and $F_a = 50$ (green).

As we can see our simulations seem to give a $\tau(q_y) \propto q_y F_a$ behavior while Cates' prediction for capillary wave decay times is $\tau(q_y) \propto q_y^3 F_a$, see ref. [10].

References

[1] B. Smit and D. Frenkel, *The Journal of Chemical Physics*, 1991, **94**, 5663–5668.

[2] S. Plimpton, *J. Comp. Phys.*, 1995, **117**, 1.

[3] G. S. Redner, A. Baskaran, and M. F. Hagan, "Reentrant phase behavior in active colloids with attraction," Phys. Rev. E, vol. 88, p. 012305, Jul 2013

[4] E. Chacón and P. Tarazona, *Phys. Rev. Lett.*, 2003, **91**, 166103.

[5] R. Delgado-Buscalioni, E. Chacón and P. Tarazona, *Phys. Rev. Lett.*, 2008, **101**, 106102.

[6] P. Tarazona, R. Checa and E. Chacón, *Phys. Rev. Lett.*, 2007, **99**, 196101.

[7] F.H. Stillinger and J. D. Weeks, *J. Phys. Chem*, 1995, **99**, 2807-2816.

[8] A.P. Williard and D. Chandler, *J. Phys. Chem. B*, 2010, **114**,1954-1958.

[9] A. Patch, D. M. Sussman, D. Yllanes and M. C. Marchetti, *Soft Matter*, 2018, **14**, 7435–7445.

[10] G. Fausti, E. Tjhung, M. E. Cates and C. Nardini, *Phys. Rev. Lett.*, 2021, **127**, 068001